Magnonic crystals with complex geometry

Anulekha De,[1] Koustuv Dutta,[1] Sucheta Mondal,[1] Saswati Barman,[2] Yoshichika Otani,[3,4] and Anjan Barman[1,*]

[1]*Department of Condensed Matter Physics and Material Sciences, S. N. Bose National Centre for Basic Sciences, Block JD, Sector III, Salt Lake, Kolkata 700106, India*

[2]*Institute of Engineering and Management, Sector V, Salt Lake, Kolkata 700 091, India*

[3]*Institute for Solid State Physics, University of Tokyo, 5-1-5 Kashiwanoha, Kashiwa, Chiba 277–8581, Japan*

[4]*RIKEN-CEMS, 2-1 Hirosawa, Wako, Saitama 351-0198, Japan*

(Received 23 November 2020; accepted 14 January 2021; published 2 February 2021)

Magnonic crystals offer a wide playground to study the emergent properties of spin waves, and ferromagnetic antidot lattices are leading candidates for magnonic devices due to the faster propagation of spin waves combined with wide-frequency tunability. Despite having a broad range of studies on periodic and quasiperiodic systems, a combination of quasiperiodic lattice with a complex basis is absent in the literature. The quasiperiodicity of octagonal lattice, along with a complex triangular antidot basis lacking reflection symmetry provides newer and richer spin-wave dynamics. Such complex magnonic crystal exhibits a strong eightfold anisotropy superposed with a weak threefold anisotropy. This is in contrast to a strong fourfold anisotropy superposed with a weak threefold anisotropy observed in a square lattice with triangular antidot basis. The spatial profiles of spin waves revealed the presence of resonant modes with both even and odd-mode quantization number, besides a mode conversion from extended to quantized mode with the systematic variation of the in-plane bias magnetic field orientation. These are in consonance with the strong anisotropic behavior of the spin-wave modes. The strong modifications of the asymmetric potential energy landscape in these magnonic crystals lead to the stark modulation of the rich spin-wave dynamics, thus opening avenues to reprogrammable magnonics with complex geometry.

DOI: 10.1103/PhysRevB.103.064402

I. INTRODUCTION

The emergence of magnonics [1–3] has promised a paradigm shift in the on-chip data communication and processing for future computing devices. Subsequent development of combination of magnonics with other systems have unearthed greater functionalities in the form of magnon spintronics [4], magphonics [5], and magnon polaritronics [6], which may give rise to next-generation devices with superior energy efficiency, speed, and miniaturization. The magnon current generated by the collective motion of magnetic moments or spin waves (SWs, quanta of which are known as magnons) does not involve the motion of charge carriers, and therefore, have lesser dissipation as compared to the spin-polarized current and even pure spin current. The short-wavelength SWs with about 50-nm wavelength has been demonstrated to propagate a distance over 60 μm with a group velocity as high as 2.6 km/s [7] and has bright future to generate miniaturized, faster, and more energy-efficient technological implementations. Further evolution of hybrid magnonics [8,9] offers the possibility of quantum transduction and quantum entanglement using magnons.

Ferromagnetic antidot lattices (ADLs) [10,11] with nonmagnetic holes periodically grooved in a continuous ferromagnetic film are of profound interest in magnonics for potential applications in designed magnon waveguides [12], filters [13], amplifiers [14], couplers [15], multiplexers [16], phase shifters [17], interferometers [18], transistors [19], as well as magnonic logic devices [20]. A flurry of investigations on standing and propagating SWs in ferromagnetic ADLs have been performed by varying a number of parameters such as antidot shape [21], lattice constant [22], lattice symmetry [23], base material [24,25], as well as the strength and orientation of the applied magnetic field [26]. Early experiments on Co ADLs showed the attenuation of uniform ferromagnetic resonance (FMR) mode due to the excitation of nonuniform SW modes [27]. Observations of field-controlled confinement, localization, and propagation of SWs [28], splitting of resonant modes [29], mode crossover [30], mode hopping [30], mode softening [31], as well as the formation of magnonic miniband [32] in ADLs, were important developments in this area.

Quasiperiodicity is an important problem in solid-state physics because quasiperiodic crystals possess long-range ordering without any periodicity, complex form of frustration leading to glassy behavior, their diffraction patterns exhibit symmetry that is forbidden by crystallographic restrictions, and they show exotic rotational symmetry [33]. Artificial quasicrystals have been extensively studied in photonics [34] and phononics [35] for a long time. Recently, magnonic quasicrystals (MQCs) [36] have become a burgeoning research topic due to various interesting properties like branching features in the band structure [37], appearance of passband [38], allowed bulk band in place of band gaps [39], etc. Concepts of self-generation of dissipative solitons in MQC active ring resonators have been reported [40]. Bhat and Grundler showed the MQCs comprising $Ni_{80}Fe_{20}$ interconnected nanobars arranged in Penrose P2, P3, and Ammann tiling exhibit distinct sets of FMR modes with eight and tenfold rotational

*abarman@bose.res.in

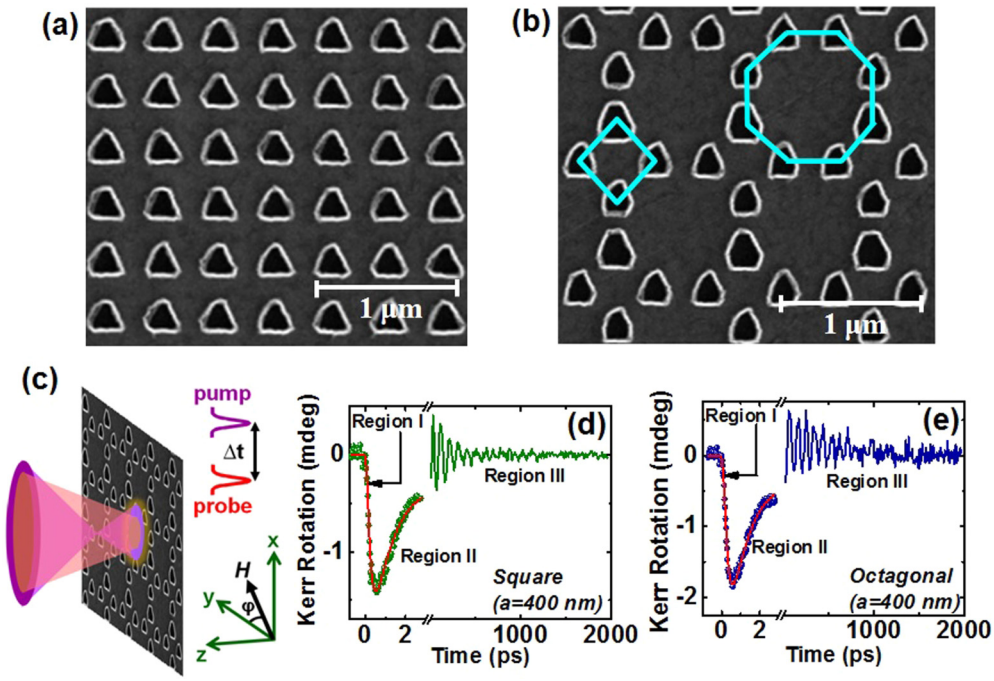

FIG. 1. SEM of the antidot lattices with (a) square and (b) octagonal symmetry. The edge length (d) of the triangular antidots is 200 nm and the lattice constant (a) is 400 nm for both lattices. The length-scale bars are shown in the images. (c) Schematic of the TR-MOKE microscope showing the pump and probe beams and the geometry of the measurement. Typical time-resolved Kerr rotation data for the (d) square and (e) octagonal lattice with $a = 400$ nm at $H = 1$ kOe and $\varphi = 0^\circ$.

symmetries with varying in-plane magnetic field orientations [41]. Experimental observation of emergent magnon motifs and Conway wormlike nanochannels in MQCs created via nanoholes arranged in Penrose P2 and P3 tiling have been reported [42]. Construction of numerous types of MQCs with Fibonacci sequences [43], and different variants of Penrose tiling, oblique tiling, Kite and Dart tiling [44], and Ammann-Beenker tiling [45,46] may offer unprecedented tunability of the SW dynamics and magnonic band structure due to the lack of translational symmetry.

MQCs in the form of octagonal lattice of ferromagnetic nanodots [47,48] and antidots [49] with broken translational symmetry have been featured in few earlier works. The whole space of an octagonal lattice cannot be covered with only one kind of tile. Instead, rhombic tiles along with octagonal tiles are required to cover the whole space. Choudhury *et al.* observed an eightfold rotational symmetry in octagonal lattice of circular-shaped $Ni_{80}Fe_{20}$ antidots [49]. Introduction of complex basis to such MQCs may result in richer and more complex SW dynamics. However, a combination of MQC with a complex basis is absent in the literature. Along with the aperiodicity of octagonal lattice we have added an asymmetric basis of triangular-shaped antidots with lack of reflection or mirror symmetry. Such complex network of antidots may be considered as an interesting testbed for providing new phenomena and stern challenges.

We report the investigation of the high-frequency SW dynamics of two-dimensional arrays of asymmetric triangular-shaped $Ni_{80}Fe_{20}$ antidots arranged in octagonal lattices with varying lattice constant. We have further compared the results with the most primitive Bravais lattice having square symmetry. A strong eightfold anisotropy superposed with a weak threefold anisotropy in the SW frequency is observed for the octagonal lattice, whereas a strong fourfold anisotropy superposed with a weak threefold anisotropy is observed for the square lattice. The micromagnetic simulations revealed a mode conversion from extended to quantized standing-wave pattern and vice versa with the variation of the orientation of the in-plane bias magnetic field. The strong modifications of the asymmetric demagnetizing regions as well as the internal-field profiles around the triangular antidots can explain the observed variation of the SW dynamics in such complex antidot lattice.

II. EXPERIMENTAL AND SIMULATION DETAILS

A. Sample fabrication

Triangular-shaped antidots were patterned on a 20-nm-thick $Ni_{80}Fe_{20}$ (Permalloy, Py hereafter) film by using a combination of electron-beam lithography (EBL), electron-beam evaporation (EBE), and ion milling [23]. The antidots with a fixed edge length (d) of 200 nm and variable lattice constants (a) of 400, 500, 600, and 700 nm are arranged in square and octagonal symmetries with total array dimensions of $25 \times 25\ \mu m^2$, as shown in the scanning electron micrographs (SEMs) of Figs. 1(a) and 1(b). Both the edge lengths and the lattice constants of these antidots suffer from $\pm 5\%$ deviations. At first a continuous Py film of 20-nm thickness was deposited on self-oxidized silicon (Si) [100] substrate by EBE at a base pressure of $\sim 2 \times 10^{-8}$ Torr. On top of the Py film, a 5-nm-thick protective layer of Al_2O_3 was deposited to protect the samples from external contamination of the

environment, degradation with time, and also from direct exposure to the femtosecond laser. A bilayer MMA/PMMA (methyl methacrylate/polymethyl methacrylate) was used for EBL to prepare the resist pattern on the continuous Py film. Finally, argon ion milling was carried out for 6 min at a base pressure of $\sim 1 \times 10^{-4}$ Torr and beam current of $\sim$60 mA to etch out the Py film from everywhere except the unexposed resist pattern to create the triangular-shaped antidots.

B. Time-resolved magneto-optical Kerr effect measurement

The ultrafast magnetization dynamics of the samples was measured by a custom-built time-resolved magneto-optical Kerr effect (TR-MOKE) microscope based upon a two-color collinear pump-probe setup [50]. A small part of the fundamental laser output ($\lambda = 800$ nm, fluence $= 2$ mJ/cm^2, pulse width $\sim$80 fs, spot size $\sim$800 nm) generated from a mode-locked Ti-sapphire laser (Tsunami, Spectra Physics) was exploited to probe the magnetization dynamics of the sample. Another part of this fundamental laser output was frequency doubled ($\lambda = 400$ nm, fluence $= 20$ mJ/cm^2, pulse width $\sim$100 fs, spot size $\sim 1\ \mu$m) and was used as the pump beam to excite the magnetization dynamics of the sample. The probe beam was time delayed with respect to the pump beam and both of them fall upon the sample collinearly through a single microscope objective (MO) with numerical aperture of 0.65. The back-reflected beams from the sample were collected by the same MO. The probe beam was steered to an optical bridge detector (OBD) after filtering out the pump beam using a spectral filter. The OBD measures the transient reflectivity and Kerr rotation by two separate lock-in amplifiers in phase-sensitive manner ensuring no breakthrough of one into another. The pump beam was modulated at 2-kHz frequency by a mechanical chopper, the frequency output of which was used as reference frequency to the lock-in amplifiers. The sample was scanned by an x-y-z piezoelectric scanning stage to position the pump and probe beams at the desired location of the ADLs. This gives high stability to the sample in the presence of feedback loops. An external magnetic field was applied at a small angle ($\sim 10^\circ$) from the sample plane, the in-plane component of which is defined as the bias magnetic field H. We varied the azimuthal angle (φ) of H between 0° and 180° during the measurement. The measurement geometry is schematically depicted in Fig. 1(c).

C. Micromagnetic simulations

The experimental data have been reproduced by finite-difference method (FDM) based micromagnetic simulations using the Object Oriented Micromagnetic Framework (OOMMF) software [51], considering arrays of 7×7 antidots for each sample to take care of the long-range magnetostatic interaction. To validate these simulation results we have also performed test simulations on the square and octagonal lattice after application of two-dimensional periodic boundary condition (2D-PBC). The test simulation results for a particular lattice constant ($a = 400$ nm) with 2D-PBC are presented in Fig. S1 of the Supplemental Material [52]. The simulations with and without application of 2D-PBC show nearly identical results. Each sample was discretized into rectangular prismlike cells with dimensions of $4 \times 4 \times 20$ nm^3, with the lateral cell size kept well below the exchange length of Py ($\approx$5.2 nm) to include the exchange interaction effect. The shapes of the triangular antidots with the actual edge roughness were derived from the SEM images. The magnetic parameters used in the simulations were exchange stiffness constant $A = 1.3 \times 10^{-6}$ erg/cm, saturation magnetization $M_s = 860$ emu/cm^3, damping coefficient $\alpha = 0.008$, gyromagnetic ratio $\gamma = 17.6$ MHz/Oe, and the magnetocrystalline anisotropy constant $K = 0$. Here, M_s, γ, and K were extracted from the Kittel fit of the bias-field dependent precession frequency of a 20-nm-thick Py blanket film deposited under the same condition as the ADLs, while A was obtained from the literature [53]. The dynamic simulations were carried out by first obtaining a static magnetic configuration under a bias magnetic field in the experimental geometry and subsequently applying a pulsed magnetic field with peak magnitude of 30 Oe, rise/fall time of 10 ps, and pulse duration of 20 ps over the whole array. For understanding the spatial nature of the observed SW modes, we further calculated the power and phase maps of these SW modes using a homebuilt MATLAB-based code named "DOTMAG" [54].

III. RESULTS AND DISCUSSION

Figures 1(d) and 1(e) show the representative time-resolved Kerr rotation traces of the square and octagonal lattice, respectively, with $d = 200$ nm and $a = 400$ nm with in-plane bias magnetic field $H = 1.0$ kOe at $\varphi = 0^\circ$. The curves reveal three important temporal regimes. Regime I corresponds to the ultrafast demagnetization (τ_M) due to the incoherent interaction after the pump pulse excites the electrons and the spin subsystems [55]. In regimes II and III, a fast relaxation (s_1) followed by a slow relaxation (s_2) occur due to the relaxation of electron and spin energies to the lattice (s_1), followed by the relaxation of lattice energy to the substrate and the surroundings (s_2) [56,57]. The damped precessional oscillation is superimposed on the slow relaxation process. We have further performed high-resolution time-resolved Kerr rotation measurements for about 3 ps from the zero delay with 25-fs temporal resolution and fitted the data with the phenomenological three-temperature model [58]. This accounts for the energy redistribution among electron, spin, and the lattice subsystems after the absorption of the laser by the electronic system, leading to an increase in the spin temperature, causing a loss of magnetization. The expression is

$$-\frac{\Delta M}{M} = \left\{ \left[\frac{A_1}{(1+t/\tau_0)^{1/2}} - \frac{A_2\tau_E - A_1\tau_M}{\tau_E - \tau_M} e^{-(t/\tau_M)} - \frac{\tau_E(A_1 - A_2)}{\tau_E - \tau_M} e^{-(t/\tau_E)} \right] H(t) + A_3\delta(t) \right\} \otimes G(t).$$

Here, A_1 represents the amplitude of magnetization after equilibrium between electron, spin, and lattice is restored, A_2 is proportional to the maximum rise in the electronic temperature and A_3 represents the state filling effects. $H(t)$ is the Heaviside step function, $\delta(t)$ is the Dirac delta function, and $G(t)$ is a Gaussian function which corresponds to the laser pulse. From the fit we have obtained $\tau_M = 209 \pm 4$ fs and

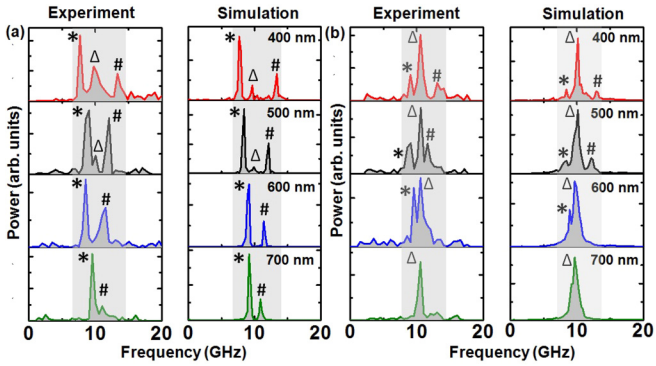

FIG. 2. The FFT power spectra of the experimental background subtracted time-resolved Kerr rotation data (left panel) along with the simulated spectra (right panel) obtained for (a) the square and (b) the octagonal lattice at $H = 1.0$ kOe and $\varphi = 0^\circ$. The lattice constants are mentioned at the right-hand side of each panel. The gray shade indicates the maximum width of the SW band for $a = 400$ nm.

226 ± 6 fs, and $s_1 = 962 \pm 10$ fs and 955 ± 9 fs for the square and octagonal lattices with $a = 400$ nm, respectively.

A. Variation of spin-wave dynamics with lattice constant

Figure 2(a) shows the fast Fourier transformed (FFT) power spectra of background-subtracted experimental time-resolved Kerr rotation data for the ADLs arranged in square symmetry with varying a, taken at $H = 1.0$ kOe and $\varphi = 0^\circ$. The square lattice with $a = 400$ nm shows a rich band of three SW modes, namely *, Δ, and # with frequencies ranging from 7.8 to 13.4 GHz. Out of these three modes, the lowest-frequency mode has relatively higher power. With the increase of a to 500 nm, we observe a frequency upshift of the modes * and Δ and a frequency downshift of the mode #. As a consequence, the width of the SW band reduces. The power of the intermediate frequency mode Δ also decreases with the increase of a. For $a = 600$ nm, the mode Δ disappears, leaving only two modes. With further increase of a to 700 nm, the frequency gap between the modes * and # decreases further and the width of the SW band is reduced further to be around 9.5 and 11.1 GHz. Figure 2(b) shows the simulated SW spectra for the square lattice in good agreement with the experimental SW spectra except for the peak width, the relative mode intensities, and peak frequencies. The slight disagreements between the experimental and simulated modes can be attributed to the difficulty in precise accounting for the detailed roughness and edge deformation of the real samples in the FDM-based micromagnetic simulations, which may give rise to complex demagnetizing regions at the edges and rounded corners of the triangular antidots. The disagreement may also arise due to the limitation in total time window to ∼2 ns taken during the experiment, while the simulated spectra are obtained for 4 ns.

Figures 2(c) and 2(d) show the experimental and simulated SW spectra, respectively, for the ADLs arranged in octagonal symmetry with varying a, taken at $H = 1.0$ kOe and $\varphi = 0^\circ$. Three clear SW modes, namely *, Δ, and #, are observed for the densest sample with $a = 400$ nm. Out of these, the intermediate frequency mode Δ has the highest power. With the increase in a (500 nm), the highest-frequency mode # undergoes a frequency downshift and merges with the Δ mode at $a = 600$ nm. The mode * also undergoes a frequency upshift with the increase in a. With further increase in a, the mode * merges with the mode Δ, leaving only a single mode at $a = 700$ nm.

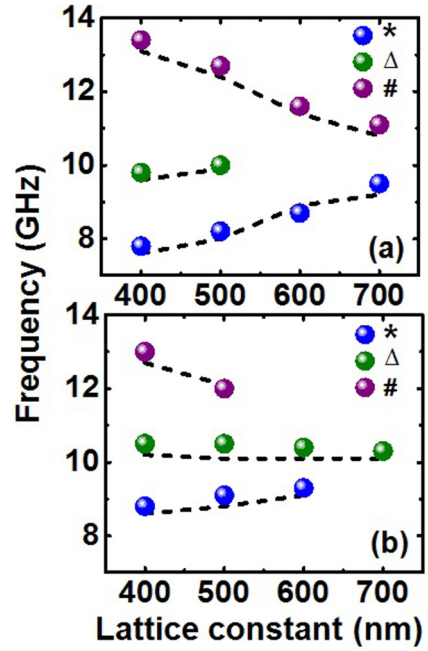

FIG. 3. Variation of SW mode frequencies of (a) the square and (b) the octagonal lattice with lattice constant (a). The solid symbols correspond to the experimental SW mode frequencies and the dashed lines represent the simulated frequencies.

Figure 3 shows the variation of the SW mode frequencies for the square and the octagonal lattice as a function of a. Figure 3(a) reveals that with the increase in a, the intermediate frequency mode Δ of the square lattice disappears and the frequency gap between the modes * and # decreases, leading to an overall reduction of the width of the SW band. On the contrary, for the octagonal lattice [Fig. 3(b)], we observe a merger of both * and # modes with the intermediate frequency mode Δ with the increase of a.

B. Micromagnetic analysis of the spin-wave mode profiles

Figure 4 shows the power and phase profiles of the SW modes for the ADLs arranged in the square and the octagonal symmetry with varying a, calculated at $H = 1.0$ kOe and $\varphi = 0^\circ$. We observe different types of extended and quantized standing SW modes for both the lattices due to the formation of confining potentials by the asymmetric demagnetizing regions around the triangular antidots. Different quantization numbers either in the backward-volume (BV) geometry or in the Damon-Eshbach (DE) geometry are assigned to the SW modes depending upon the number of antinodes.

Figures 4(a) and 4(b) show the power and phase profiles, respectively, for the SW modes of the square lattice. In order to maintain the uniformity in describing the nature of the observed standing SW modes, we have assigned quantization number n for the modes forming standing waves in the region

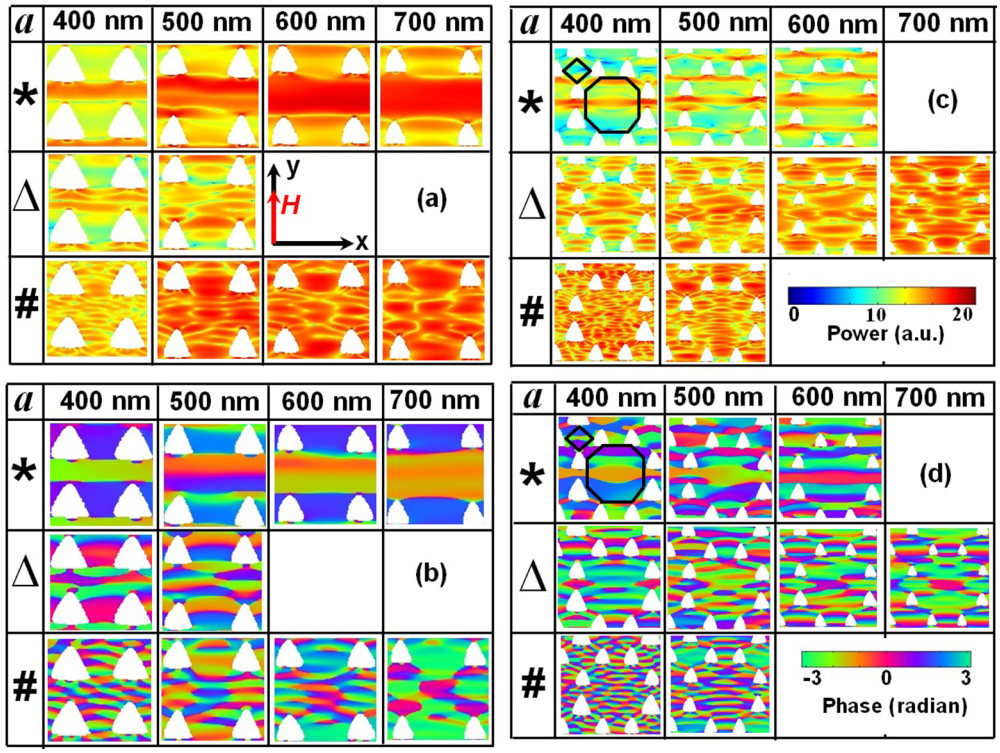

FIG. 4. Simulated power and phase maps of different SW modes obtained at $H = 1.0$ kOe applied at $\varphi = 0°$, for the ADLs. The color bars are shown inside the figure. (a) Power and (b) phase profiles for the square lattice and (c) power and (d) phase profiles for the octagonal lattice with varying a.

between the two consecutive antidots along the y direction. It is evident that the mode * for the square lattice with $a = 400$ nm has an extended nature between the neighboring antidot rows along the x direction, i.e., in the DE geometry. The mode Δ also extends through the channel while forming a standing-wave pattern with $n = 3$ between two consecutive antidot rows. For these two modes negligible power outside the channels is observed. The mode # forms a criss-cross-like pattern with an even quantization number ($n = 4$).

It is worth mentioning that inside the channels between the neighboring antidot rows in the x direction, the potential is not symmetric due to the occurrence of base of a triangle on one side and vertex of another triangle on the other side. Generally, in a symmetric potential, odd modes (with odd number of nodal planes) are observed, whereas asymmetric potential can accommodate even modes too [59]. For $a = 500$ nm, the mode * has an extended nature in the DE geometry along the channels between the neighboring antidot rows along the x direction with a mixed BV nature with $n = 2$. The mode Δ has $n = 5$, whereas the mode # is again a criss-cross-like mode with $n = 6$. The mode * has a similar mixed DE-BV nature along the channels with $n = 2$ and 3 for both $a = 600$ and 700 nm, respectively. On the other hand, mode # shows criss-cross-like nature with $n = 7$ and 3 for $a = 600$ and 700 nm, respectively. It is to be noted that power of mode # is located both in the channels and the space between the two consecutive antidots along the x direction. Notably the spatial uniformity of the power of mode # increases with the increase in a, while the phase profile indicates a gradual conversion from a more quantized mode to a more uniform mode with the increase in a. This may explain the gradual decrease in the frequency of mode #, which eventually approaches that of mode *.

The power and phase profiles of the SW modes for the octagonal lattice are presented in Figs. 4(c) and 4(d). In this case, depending upon the confinement region of the SWs, two different quantization numbers, m and n, are assigned. The quantization of SWs along the y direction inside the octagonal unit defined by the black octagonal box is represented by m, while the quantization of the SWs along the y direction inside the rhombic unit between two such consecutive octagonal units defined by the black rhombic box is represented by n. The modes are generally localized but some modes extend through the available channels in between the neighboring antidots. The mode numbers (m, n) for the mode * are (5, 3), (6, 3) and (7, 4) for $a = 400$, 500, and 600 nm, respectively. Due to the asymmetric potential and the complex lattice geometry, the width of this mode is modulated along the channel in the x direction. The mode Δ has (m, n) of (11, 5), (11, 5), (9, 6), and (7, 4) for $a = 400$, 500, 600, and 700 nm, respectively. The mode # has (m, n) of (19, 7) and (15, 3) for $a = 400$ and 500 nm, respectively. Both the Δ and # modes form complex criss-cross pattern both within the octagonal and rhombic units. With the increase in a, the quantization number of mode # decreases inside the octagonal unit, while it transforms from highly quantized to nearly uniform mode in the rhombic unit. This may explain the decrease in frequency of this mode with the increase in a. The phase profiles of the Δ mode also become more uniform with the increase in a. The spatial power profiles of these two modes also become more

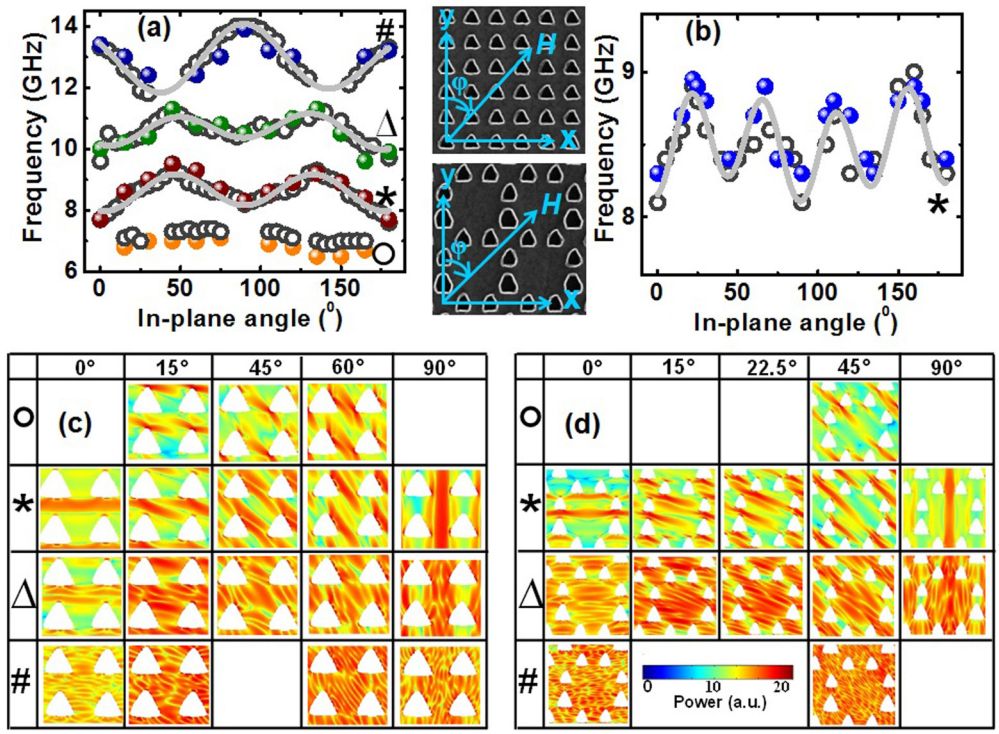

FIG. 5. Variation of SW frequencies with the azimuthal angle (φ) of H varying from 0° to 180° for (a) the square and (b) the octagonal lattice symmetry with $a = 400$ nm at $H = 1.0$ kOe. The solid symbols represent the experimental data points and the hollow symbols represent the simulated data points. The solid lines describe the sinusoidal fits for the observed anisotropic SW modes. Simulated power profiles of the SW modes for (c) the square and (d) the octagonal lattice symmetry with $a = 400$ nm at some specific values of φ. The color bar is shown inside the figure.

uniform. Consequently, their frequencies decrease and seem to approach that of mode *.

For the ADL with square symmetry, the lowest-frequency mode *, having an extended nature through the nanochannels, possesses the highest power. This is attributed to the fact that SW extension through the nanochannels within the neighboring antidot rows occurs most naturally for the square lattice. On the contrary, SW localization within the octagonal and rhombic units occurs most naturally for the octagonal lattice due to the scarcity of nanochannels allowing the SW propagation. Consequently, the intermediate frequency mode Δ having more localized nature appears with highest power as opposed to the lower or higher-frequency modes.

C. Anisotropic variation of the spin-wave modes

To investigate the SW anisotropy in these samples, we have measured the SW dynamics of the square and octagonal lattices ($a = 400$ nm), by varying the azimuthal angle (φ) of the bias magnetic field at a fixed strength of $H = 1.0$ kOe. The bias magnetic field (H) dependence of the SW frequencies at $\varphi = 0^\circ$ and the experimental and simulated FFT power spectra at different values of φ for these samples are presented in Figs. S2 and S3, respectively, of the Supplemental Material [52]. The angular dispersions of the precessional frequencies of different SW modes as a function of φ varying from 0° to 180° for the square lattice are shown in Fig. 5(a). The solid symbols represent the experimental frequencies, the hollow symbols represent the simulated frequencies, while the solid lines correspond to the theoretical fits using harmonic functions with different rotational symmetries. It is clear that while the * and Δ modes appear for almost all values of φ, the # mode shows a discontinuous angular dispersion appearing only for $0^\circ \leqslant \varphi \leqslant 25^\circ$ and $55^\circ \leqslant \varphi \leqslant 90^\circ$ and disappearing in between. The modes *, Δ, and # exhibit a stronger fourfold anisotropy superposed with a weaker threefold anisotropy, while the rotational anisotropy of the highest-frequency mode (#) is in opposite phase with the other two modes. A combination of triangular-shaped antidots arranged on square lattice symmetry gives rise to the observed three- and fourfold rotational anisotropy in the SW frequencies of these modes. The anisotropic behavior of the frequency of mode * of the octagonal lattice is shown in Fig. 5(b). The mode * possesses a superposition of strong eightfold and weak threefold anisotropies. The other modes do not exhibit any specific anisotropic behavior. The eightfold rotational anisotropy arises from the octagonal lattice symmetry, whereas the weak threefold anisotropy arises due to the triangular shape of the antidots. The eightfold symmetry is a signature of the quasiperiodicity of the octagonal lattice as reported before [49].

The power profiles of the SW modes for the square and octagonal lattice are shown in Figs. 5(c) and 5(d), respectively. The mode * for both the lattices undergoes significant modification with the variation of φ. This mode for the square lattice, having an extended nature at $\varphi = 0^\circ$, converts

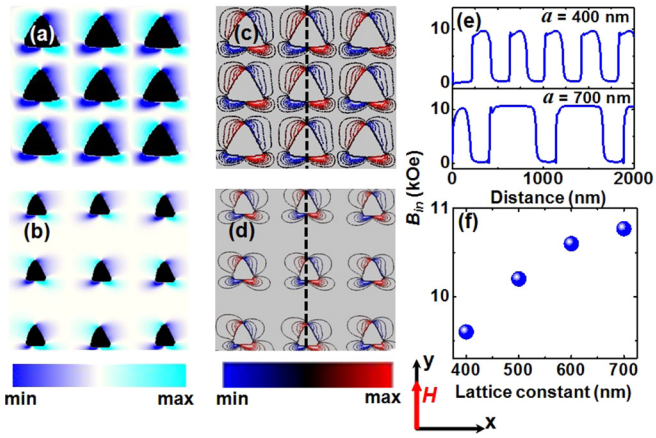

FIG. 6. Magnetization maps for the square lattice with (a) $a = 400$ nm and (b) $a = 700$ nm. Contour plots of the simulated internal-field distributions for the square lattice with (c) $a = 400$ nm and (d) $a = 700$ nm. The corresponding color maps and the schematic of H are shown at the bottom of the figure. (e) Line scans of the simulated internal field (B_{in}) of the two lattices taken along the dotted lines as shown in (c) and (d). The values of a are mentioned in the figure. (f) The variation of B_{in} with a.

into quasiextended and localized modes for the intermediate angle before converting back to a flipped extended mode for $\varphi = 90°$. This behavior is repeated periodically in consonance with the observed fourfold rotational anisotropy of this mode. For the octagonal lattice, the mode * also exhibits SW mode conversion between extended and quasiextended modes having extended nature at 0°, 45°, and 90°. This behavior is again repeated periodically in consonance with the observed eightfold rotational anisotropy of this mode.

The mode Δ shows extended nature for $\varphi = 0°$ and 90°, while being purely localized at 45° in the square lattice. However, this mode shows a peculiar behavior in the octagonal lattice, being extended at 45° and 90°, while being localized at 0°. Apparently, this is due to the lack of channel formation due to the demagnetizing field around the triangular holes at 0°. The criss-cross-like mode # also shows a mode conversion between extended (0° and 90°) and localized modes (intermediate angles) in square lattice but no apparent mode conversion is observed in the octagonal lattice for this mode. For both square and octagonal symmetries, a new mode ○ appears in the lower-frequency regime at some specific values of φ, with its power primarily concentrated at the sharp corners of the triangular antidots. This mode appears mainly due to the asymmetric demagnetizing regions around the triangular antidots and does not show any specific anisotropic behavior. The appearance of such lower-frequency edge-localized mode in triangular antidots has been reported earlier [60].

D. Magnetostatic field distribution

In order to gain more insights into the variation of the SW modes with varying a in these ADLs with square and octagonal symmetry, we have calculated the magnetization maps and the magnetostatic field distributions of these lattices using the LLG micromagnetics simulator [61]. The magnetization maps (domain plot) around the triangular antidots for the square lattice with different a, at $H = 1.0$ kOe are shown in Figs. 6(a) and 6(b), whereas the contour plots of simulated internal field distributions are shown in Figs. 6(c) and 6(d). The internal-field lines around the antidots clearly indicate an asymmetric potential across the channel of extension of the SWs. The demagnetizing regions, as well as the density of field lines around the antidots reduce with the increase in a. The internal field strengths (B_{in}) are obtained by taking line scans along the dashed lines in the y direction as shown in Figs. 6(c) and 6(d). Figure 6(e) shows the variation of B_{in} with distance for $a = 400$ and 700 nm. It is evident from Fig. 6(f) that B_{in} increases significantly from ∼9.6 to ∼10.7 kOe with the increase in a within the channels of SW extension due to the systematic decrease in the overlapping between the demagnetizing fields around the antidots. The increase in B_{in}

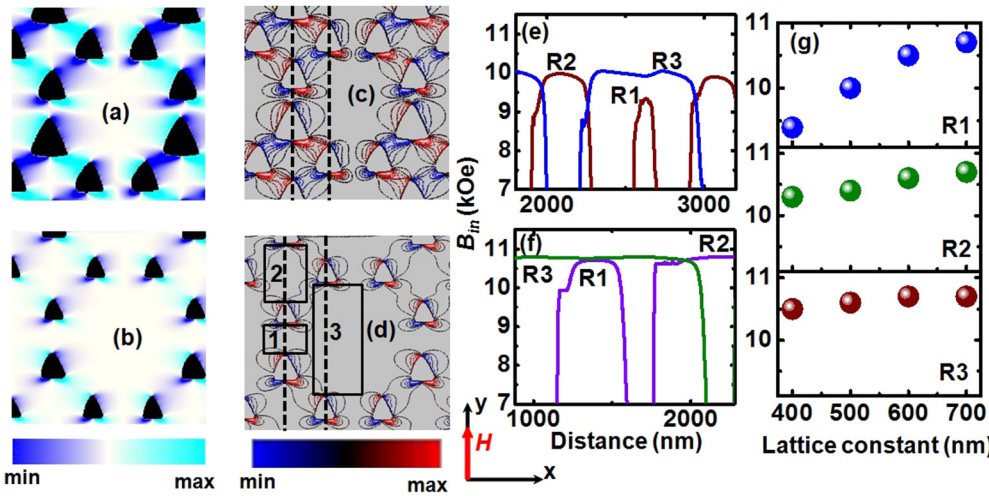

FIG. 7. Magnetization maps for the octagonal lattice with (a) $a = 400$ nm and (b) $a = 700$ nm. Contour plots of the simulated internal-field distributions for the octagonal lattice with (c) $a = 400$ nm and (d) $a = 700$ nm. The corresponding color maps and the schematic of H are shown at the bottom of the figure. Line scans of the simulated internal field (B_{in}) for (e) $a = 400$ nm and (f) $a = 700$ nm taken along the black dotted lines as shown in (c) and (d). (g) The variation of B_{in} with a, at three different regions as shown by black boxes in (d).

with a is responsible for the similar increase in the frequencies of modes * and Δ with a as observed in Fig. 3(a).

We have further investigated the magnetization maps [Figs. 7(a) and 7(b)] and the contour plots of simulated internal-field distributions [Figs. 7(c) and 7(d)] for the octagonal lattice for different values of a, at $H = 1.0$ kOe. We have calculated the B_{in} by taking line scans in different region of the lattice as shown in Figs. 7(c) and 7(d). It is evident from Fig. 7(e) that for the densest octagonal lattice with $a = 400$ nm, B_{in} is significantly lower ($\sim$9.3 kOe) in region 1 as compared to the regions 2 ($\sim$10.5 kOe) and 3 ($\sim$10.3 kOe). This prominent modification in B_{in} arises from the overlapping of complex demagnetizing field in this dense lattice having different magnetic environment in different regions stemming from its octagonal symmetry as well as triangular holes. However, due to the decrease in the overall effective demagnetizing fields, B_{in} increases with a, and becomes identical in all three regions [Fig. 7(f)] at $a = 700$ nm, leading towards the merging of the three modes *, Δ, and # to a single mode for $a = 700$ nm. The variations of B_{in} with a in all three regions of the octagonal lattice are shown in Fig. 7(g). The sharp increase in B_{in} with a in region 1 (channel) is responsible for the increase in frequency of the mode * with a. On the contrary, B_{in} increases very gently with a inside region 2 (rhombic unit) and remains nearly constant inside region 3 (octagonal unit). This might be responsible for the negligible variation of the frequency of mode Δ with a.

IV. SUMMARY

In summary, we have studied antidot magnonic crystals with complex geometry in the form of octagonal lattice with a triangular-shaped basis lacking reflection symmetry and compared its SW dynamics with that of a square lattice. Rich multimodal SW spectra are obtained for the most densely packed lattice, whereas the number of SW modes reduces systematically with the increase in lattice constant approaching towards a nearly thin-film-like behavior due to the reduction of the demagnetizing field around the antidots in both lattice symmetries. A combination of the triangular-shaped antidots arranged in octagonal symmetry exhibits a strong eightfold anisotropy superposed with a weak threefold anisotropy, whereas a strong fourfold anisotropy superposed with a weak threefold anisotropy is observed in the square lattice. The experimental observations have been reproduced by micromagnetic simulations and the spatial profiles of the anisotropic SW modes unveiled mode conversion between extended, quasiextended, and quantized standing SW modes with the variation of in-plane bias magnetic field orientation, along with the appearance of some localized edge modes at some specific bias magnetic field orientation due to the presence of the sharp triangular corners of the antidots. The internal fields including the demagnetization field distributions interpret the origin of the observed SW modes. Our findings offer opportunities in magnonic crystals with complex geometry that are expected to provide exotic SW propagation properties to pave the way for the advancement of reprogrammable magnonics.

ACKNOWLEDGMENTS

The authors gratefully acknowledge Arundhati Adhikari for assistance. A.B. acknowledges the financial assistance from the S. N. Bose National Centre for Basic Sciences under Project No. SNB/AB/18-19/211. A.D., K.D., and S.M. acknowledge DST, Govt. of India for the INSPIRE fellowship. S.B. acknowledges Science and Engineering Research Board (SERB) for funding under Grant No. CRG/2018/002080.

[1] S. Neusser and D. Grundler, Adv. Mater. **21**, 2927 (2009).
[2] V. V. Kruglyak, S. O. Demokritov, and D. Grundler, J. Phys. D: Appl. Phys. **43**, 264001 (2010).
[3] B. Lenk, H. Ulrichs, F. Garbs, and M. Münzenberg, Phys. Rep. **507**, 107 (2011).
[4] A. V. Chumak, V. I. Vasyuchka, A. A. Serga, and B. Hillebrands, Nat. Phys. **11**, 453 (2015).
[5] P. Graczyk and M. Krawczyk, Phys. Rev. B **96**, 024407 (2017).
[6] W. Yu, T. Yu, and G. E. W. Bauer, Phys. Rev. B **102**, 064416 (2020).
[7] C. Liu, J. Chen, T. Liu, F. Heimbach, H. Yu, Y. Xiao, J. Hu, M. Liu, H. Chang, T. Stueckler, S. Tu, Y. Zhang, Y. Zhang, P. Gao, Z. Liao, D. Yu, K. Xia, N. Lei, W. Zhao, and M. Wu, Nat. Commun. **9**, 738 (2018).
[8] D. L. Quirion, Y. Tabuchi, A. Gloppe, K. Usami, and Y. Nakamura, Appl. Phys. Express **12**, 070101 (2019).
[9] Y. Li, W. Zhang, V. Tyberkevych, W. K. Kwok, A. Hoffmann, and V. Novosad, J. Appl. Phys. **128**, 130902 (2020).
[10] S. Neusser, B. Botters, and D. Grundler, Phys. Rev. B **78**, 054406 (2008).
[11] P. Vavassori, G. Gubbioti, G. Zangari, C. T. Yu, H. Yin, H. Jiang, and G. J. Mankey, J. Appl. Phys. **91**, 7992 (2002).
[12] V. E. Demidov, M. P. Kostylev, K. Rott, J. Münchenberger, G. Reiss, and S. O. Demokritov, Appl. Phys. Lett. **99**, 082507 (2011).
[13] S. K. Kim, K. S. Lee, and D. S. Han, Appl. Phys. Lett. **95**, 082507 (2009).
[14] Y. Acremann, X. W. Yu, A. A. Tulapurkar, A. Scherz, V. Chembrolu, J. A. Katine, M. J. Carey, H. C. Siegmann, and J. Stohr, Appl. Phys. Lett. **93**, 102513 (2008).
[15] H. Yu, G. Duerr, R. Huber, M. Bahr, T. Schwarze, F. Brandl, and D. Grundler, Nat. Commun. **4**, 2702 (2013).
[16] K. Vogt, F. Y. Fradin, J. E. Pearson, T. Sebastian, S. D. Bader, B. Hillebrands, A. Hoffmann, and H. Schultheiss, Nat. Commun. **5**, 3727 (2014).
[17] Y. Au, M. Dvornik, O. Dmytriiev, and V. V. Kruglyak, Appl. Phys. Lett. **100**, 172408 (2012).
[18] K. S. Lee and S. K. Kim, J. Appl. Phys. **104**, 053909 (2008).
[19] A. V. Chumak, A. A. Serga, and B. Hillebrands, Nat. Commun. **5**, 4700 (2014).
[20] T. Schneider, A. A. Serga, B. Leven, and B. Hillebrands, Appl. Phys. Lett. **92**, 022505 (2008).
[21] R. Mandal, P. Laha, K. Das, S. Saha, S. Barman, A. K. Raychaudhuri, and A. Barman, Appl. Phys. Lett. **103**, 262410 (2013).

[22] R. Mandal, S. Saha, D. Kumar, S. Barman, S. Pal, K. Das, A. K. Raychaudhuri, Y. Fukuma, Y. Otani, and A. Barman, ACS Nano **6**, 3397 (2012).

[23] R. Mandal, S. Barman, S. Saha, Y. Otani, and A. Barman, J. Appl. Phys. **118**, 053910 (2015).

[24] S. Pal, J. W. Klos, K. Das, O. Hellwig, P. Gruszecki, M. Krawczyk, and A. Barman, Appl. Phys. Lett. **105**, 162408 (2014).

[25] S. Mallick, S. Mondal, T. Seki, S. Sahoo, T. Forrest, F. Maccherozzi, Z. Wen, S. Barman, A. Barman, K. Takanashi, and S. Bedanta, Phys. Rev. Appl. **12**, 014043 (2019).

[26] A. De, S. Mondal, S. Sahoo, S. Barman, Y. Otani, R. K. Mitra, and A. Barman, Beilstein J. Nanotechnol. **9**, 1123 (2018).

[27] O. N. Martyanov, V. F. Yudanov, R. N. Lee, S. A. Nepijko, H. J. Elmers, R. Hertel, C. M. Schneider, and G. Schonhense, Phys. Rev. B **75**, 174429 (2007).

[28] S. Neusser, B. Botters, M. Becherer, D. Schmitt-Landsiedel, and D. Grundler, Appl. Phys. Lett. **93**, 122501 (2008).

[29] K. Adhikari, S. Barman, R. Mandal, Y. Otani, and A. Barman, Phys. Rev. Appl. **10**, 044010 (2018).

[30] S. Choudhury, S. Majumder, S. Barman, Y. Otani, and A. Barman, Phys. Rev. Appl. **10**, 064044 (2018).

[31] F. Montoncello, L. Giovannini, and M. Krawczyk, J. Appl. Phys. **112**, 033911 (2012).

[32] S. Neusser, G. Duerr, S. Tacchi, M. Madami, M. L. Sokolovskyy, G. Gubbiotti, M. Krawczyk, and D. Grundler, Phys. Rev. B **84**, 094454 (2011).

[33] D. Levine and P. J. Steinhardt, Phys. Rev. B **34**, 596 (1986).

[34] M. C. Rechtsman, H. C. Jeong, P. M. Chaikin, S. Torquato, and P. J. Steinhardt, Phys. Rev. Lett. **101**, 073902 (2008).

[35] A. L. Chen, Y. S. Wang, Y. F. Guo, and Z. D. Wang, Solid State Commun. **145**, 103 (2008).

[36] D. Shi, Z. Budrikis, A. Stein, S. A. Morley, P. D. Olmsted, G. Burnell, and C. H. Marrows, Nat. Phys. **14**, 309 (2018).

[37] C. H. Chen, R. Z. Qiu, C. H. Chang, and W. J. Hsueh, AIP Adv. **4**, 087102 (2014).

[38] C. H. O. Costa, M. S. Vasconcelos, and E. L. Albuquerque, J. Appl. Phys. **109**, 07D319 (2011).

[39] C. H. O. Costa, M. S. Vasconcelos, P. H. R. Barbosa, and F. F. Barbosa Filho, J. Magn. Magn. Mater. **324**, 2315 (2012).

[40] S. V. Grishin, E. N. Beginin, M. A. Morozova, Y. P. Sharaevskii, and S. A. Nikitov, J. Appl. Phys. **115**, 053908 (2014).

[41] V. S. Bhat and D. Grundler, Phys. Rev. B **98**, 174408 (2018).

[42] S. Watanabe, V. S. Bhat, K. Baumgaert, and D. Grundler, Adv. Funct. Mater. **30**, 2001388 (2020).

[43] F. Lisiecki, J. Rychły, P. Kuświk, H. Głowiński, J. W. Kłos, F. Groß, N. Träger, I. Bykova, M. Weigand, M. Zelent, E. J. Goering, G. Schütz, M. Krawczyk, F. Stobiecki, J. Dubowik, and J. Grafe, Phys. Rev. Appl. **11**, 054061 (2019).

[44] B. Farmer, V. S. Bhat, A. Balk, E. Teipel, N. Smith, J. Unguris, D. J. Keavney, J. T. Hastings, and L. E. De Long, Phys. Rev. B **93**, 134428 (2016).

[45] M. Senechal, *Quasicrystals and Geometry* (Cambridge University Press, Cambridge, 1996).

[46] M. Gardner, *Penrose Tiles to Trapdoor Ciphers: And the Return of Dr Matrix, MAA Spectrum, Mathematical Association of America, Spectrum Series* (Cambridge University Press, Cambridge, 1997), p. 41.

[47] S. Saha, R. Mandal, S. Barman, D. Kumar, B. Rana, Y. Fukuma, S. Sugimoto, Y. Otani, and A. Barman, Adv. Funct. Mater. **23**, 2378 (2013).

[48] S. Mondal, S. Barman, S. Choudhury, Y. Otani, and A. Barman, J. Magn. Magn. Mater. **458**, 95 (2018).

[49] S. Choudhury, S. Barman, Y. Otani, and A. Barman, ACS Nano **11**, 8814 (2017).

[50] A. Barman and A. Haldar, Solid State Phys. **65**, 1 (2014).

[51] M. Donahue and D. G. Porter, NIST Interagency Report No. 6376 (National Institute of Standard and Technology, Gaithersburg, MD, 1999) http://math.nist.gov/oommf.

[52] See Supplemental Material at http://link.aps.org/supplemental/10.1103/PhysRevB.103.064402 containing **S1.** Micromagnetic simulations with two-dimensional periodic boundary condition, **S2.** Bias magnetic field dependence of the spin-wave frequencies and **S3.** Variation of spin-wave spectra with the azimuthal angle (φ) of the bias magnetic field.

[53] K. H. J. Buschow, *Handbook of Magnetic Materials* (North Holland, Amsterdam, Netherlands, 2009), Vol. 18, p. 168.

[54] D. Kumar, O. Dmytriiev, S. Ponraj, and A. Barman, J. Phys. D: Appl. Phys. **45**, 015001 (2012).

[55] E. Beaurepaire, J.-C. Merle, A. Daunois, and J.-Y. Bigot, Phys. Rev. Lett. **76**, 4250 (1996).

[56] A. Laraoui, J. Venuat, V. Halte, M. Albrecht, E. Beaurepaire, and J.-Y. Bigot, J. Appl. Phys. **101**, 09C105 (2007).

[57] A. Barman and J. Sinha, *Spin Dynamics and Damping in Ferromagnetic Thin Films and Nanostructures* (Springer International Publishing AG, 2018).

[58] U. Atxitia, O. Chubykalo-Fesenko, J. Walowski, A. Mann, and M. Münzenberg, Phys. Rev. B **81**, 174401 (2010).

[59] B. K. Mahato, B. Rana, D. Kumar, S. Barman, S. Sugimoto, Y. Otani, and A. Barman, Appl. Phys. Lett. **105**, 012406 (2014).

[60] A. De, S. Mondal, S. Choudhury, S. Sahoo, S. Majumder, S. Barman, Y. Otani, and A. Barman, J. Magn. Magn. Mater. **487**, 165263 (2019).

[61] LLG Micromagnetics Simulator, developed by M. R. Scheinfein, http://llgmicro. home.mindspring.com (accessed March 8, 2018).